Inclusive γ, π^0, K^0, and Λ production in 12.4-GeV/c pp interactions

K. Jaeger, J. Campbell,* G. Charlton,† and D. Swanson
Argonne National Laboratory, Argonne, Illinois 60439‡

C. Fu and H. A. Rubin
Illinois Institute of Technology, Chicago, Illinois 60616 §

R. G. Glasser
University of Maryland, College Park, Maryland 20742‡

D. Koetke
Concordia Teachers College, River Forest, Illinois 60305‡

J. Whitmore
Fermi National Accelerator Laboratory, Batavia, Illinois 60510 ||

(Received 16 September 1974)

In an exposure of the Argonne National Laboratory 12-foot hydrogen bubble chamber to a beam of 12.4-GeV/c protons, we have measured the total and differential cross sections for the inclusive reactions $p + p \to \gamma + X$, $\pi^0 + X$, $K^0 + X$, and $\Lambda + X$, as well as estimates for the inclusive η and Σ^0 cross sections. We present the average number of π^0, K^0, and Λ as a function of the associated charge multiplicity. We observe that the average charge multiplicity in pp collisions is the same whether or not a π^0, K^0, or Λ is also produced in the interaction. Invariant cross sections are presented as a function of P_T^2 and x, the Feynman scaling variable. The π^0 differential cross sections are consistent with the relation $d\sigma/dP(\pi^0) = \frac{1}{2}[d\sigma/dP(\pi^+) + d\sigma/dP(\pi^-)]$ for all pion momenta P. The differential cross section for Λ production indicates a break in the distribution of $|t - t_{\min}| = 1.4$ (GeV/c)^2. The polarization of the Λ's is found to be consistent with zero for all values of x.

I. INTRODUCTION

This paper presents results of the inclusive γ, π^0, $K^0/\bar{K}^0$, and Λ (including those from Σ^0 decays) production from 12.4-GeV/c pp interactions, using the hydrogen-filled Argonne National Laboratory 12-foot bubble chamber. Since this film constitutes the first exposure of the large bubble chamber, pictures were accumulated starting with the initial tune-up. Over a period of eight months, 100 000 pictures were obtained, of which 50 000 were retained as usable four-view photographs. The rest had to be rejected for reasons such as poor beam quality, too many tracks in the chamber, too much dirt in the chamber, one or more camera failures, etc. In this analysis we present the data from 26 300 pictures.

With an average of six beam tracks per picture, the present film sample corresponds to 1.21 ±0.06 events/μb for the K^0 or Λ events. Owing to a smaller fiducial volume, the γ events correspond to a film sample of 1.05 ±0.05 events/μb. Since most results from the inclusive γ and π^0 production have already been published,[1,2] this paper will concentrate on the detailed description of the experiment and on the inclusive Λ and $K^0/\bar{K}^0$ production.

II. EXPERIMENTAL ARRANGEMENT

A. The proton beam

About 10^9 protons/pulse were extracted from the Zero Gradient Synchrotron (ZGS). By use of two quadrupoles, set for maximum defocusing in both the horizontal and vertical planes, as well as two collimators, the beam flux was reduced to an average of 6 protons/pulse. In order to spread the beam horizontally over 91 cm and vertically up to 10 cm at the chamber beam window, three additional quadrupole magnets were employed. Two were located 105 m upstream from the chamber and the third quadrupole was about 60 m from the chamber.[3]

B. The 12-foot bubble chamber

This exposure constitutes the first hadron experiment performed with the 12-foot bubble chamber (cross-sectional view in Fig. 1). The total enclosed volume of hydrogen is 26.3 m^3 of which 15.5 m^3 is visible by four cameras. The inside of the chamber is lined with aluminum panels covered with Scotchlite, allowing bright field illumination. The side panels define an average

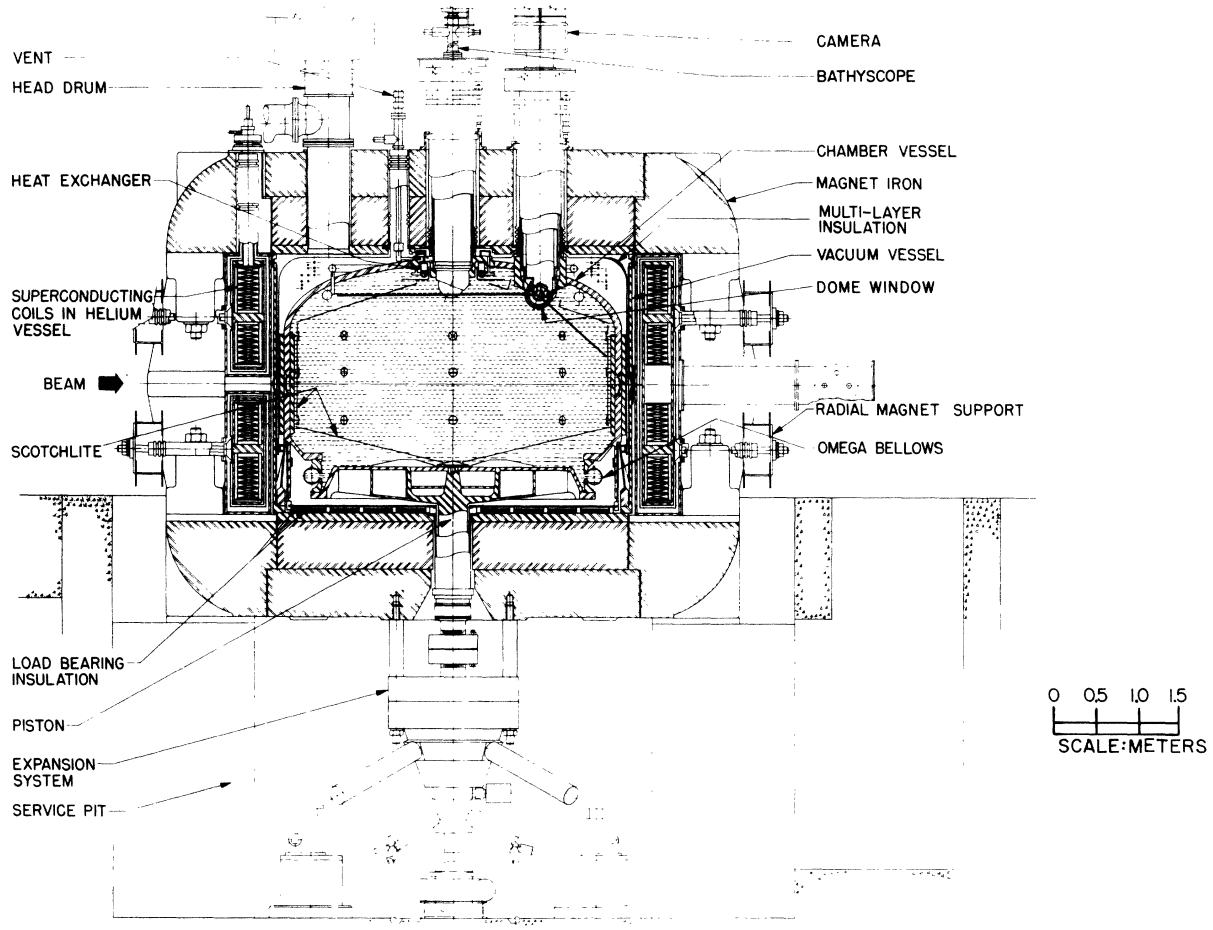

FIG. 1. Cross-sectional view of the 12-foot bubble chamber.

chamber diameter of 376 cm. A total of 24 fiducial marks are mounted on the chamber circumference, of which 16 were used for reconstruction purposes.

Two wires were stretched across the bottom of the chamber and parallel to the incoming beam. They were initially used to simulate beam tracks for tests of the optical system and the track reconstruction programs. It was decided to leave the wires installed in the chamber during this experiment since they gave a convenient indication of a straight line projection onto film. As such, they were helpful for pointing neutral secondary events back to a primary vertex. The wires were also helpful in distinguishing beam tracks from off-beam tracks and for determining the direction of curvature of secondary tracks.

The origin of the chamber coordinate system is located at the center of the plane defined by the four camera lenses. The z axis points downward perpendicular to this plane and the x and y axes then form a right-handed system, with the beam aimed along the x axis. The entire volume with $z > 50$ cm is in focus to all cameras. The nominal beam plane is at $z = 132$ cm.

The magnetic field in the chamber is produced by a superconducting magnet, the first to be used with a large bubble chamber. For this experiment, the nominal field at the center of the chamber was 15.1 kG. Field maps at 10, 15, and 18 kG were obtained by use of flip coils and nuclear-magnetic-resonance probes. Polynomial fits to these measurements yielded fits which agree with the maps to within 0.1% over the entire fiducial volume.[4]

III. DATA REDUCTION

A. Scanning machines

The film was scanned on three-view conventional tables equipped with 12× magnification optics as well as machines which were built or modified

specifically for 12-foot bubble chamber film. These latter tables were equipped with optical systems with both high (72×) and low (12×) magnification as well as with film transport systems that would properly display and simultaneously move all four views of the 70-mm film. The high magnification turned out to be a very useful option for studying detailed regions in the chamber during scanning. It should be noted that the demagnification of the beam plane from space onto film for any one camera varies from ~40 for the region just underneath the camera to ~110 for the region on the opposite side of the chamber.

B. Scanning rules

The scanning process consisted of searching for any neutral particle interaction, scatter, decay, or conversion. In order to categorize the "neutral" events, they were separated into two groups: V^0's and neutron stars. The latter are interactions of secondary neutrons in the hydrogen, producing 3, 5, 7, or 9 charged particles, and will not be discussed here.

When a V^0 event was found, the scanner tried to locate a beam interaction vertex from which it may have originated. Because of the optical distortions of the 12-foot bubble chamber cameras (the lenses have a 140° field of view), the pointing test had to be considerably relaxed and any primary vertex that was found near the V^0 line of flight was considered a V^0 production vertex candidate. Both the primary and V^0 vertices were then digitized to an accuracy of about 100 μ on film. The (x,y) coordinates so obtained allowed the operator of the computer-controlled measuring machine, POLLY III,[5] to locate and to measure the event quickly.

The number of beam tracks that passed through the entry to a fiducial volume was counted on every tenth frame. A beam track was defined as a track that had little curvature and traveled "roughly parallel" to similar tracks entering through the beam window. This criterion was well enough defined to eliminate most off-beam tracks and to allow experienced scanners to agree on the beam count to within the quoted errors.

For this experiment, a total of 19100 pictures were double-scanned and 7200 were single-scanned in about eight months at Argonne National Laboratory (ANL) and Illinois Institute of Technology (IIT). The average scanning rate for both the ANL and IIT scanning teams was about 30 frames/hour with a maximum rate of 40–50 frames/hour with acceptable efficiency. The scanners digitized on the average about one vertex per scanned picture.

C. Measuring

The selected events were measured on the ANL POLLY III measuring machine.[5] Using the predigitized coordinate of each relevant vertex on the film, POLLY III measured the V^0 events at a rate of approximately 30 per hour with a 60% pass rate for the first measurement. In 26 300 pictures, we found 11 595 V^0's with 13 141 possible primary vertices.

D. Data processing

The measurements were processed through the three-view geometry program TVGP and the kinematics fitting program SQUAW. The TVGP experiment-dependent constants, setting error and angle error floors, were determined from reconstructed fiducial maps and from stretch plots. The setting error for POLLY III measurements was found to be 5 μ on film.[4] To determine the proper angle floors, a sample of four-prong events was measured on POLLY III and reconstructed in TVGP. Using those events that fit the reaction $pp \to pp\pi^+\pi^-$, the angle error floors were adjusted until the stretch plots were centered at zero with unit width, and a uniform four-constraint probability distribution was obtained. The angle error floors for azimuth (ϕ) and dip (λ) thus determined were 0.09 and 0.05 degrees, respectively.

Primary and secondary vertices were required to have a single point reconstruction error of less than 50 μ on the film. The rms deviation on the film of all measured points from the reconstructed track was required to be less than 25 μ. Events not meeting these requirements were remeasured on POLLY III. After four measurements on POLLY III, 84% of the V^0's and 93% of the primary vertices had passed the criteria.

The TVGP output was then processed by a program called NMERGE, which took the laboratory angles for each reconstructed "neutral" event at a secondary vertex and compared them, with a loose tolerance, to the laboratory angles of all possible two-point tracks joining each of the primary vertices with the secondary vertex. NMERGE did this for all of the "neutral" events on the frame and assembled possible candidates into "complete" events for processing in SQUAW.

For cases where a "neutral" event pointed to a primary vertex, the following fits were attempted by SQUAW:

$$\gamma p_s \to e^+e^-p_s, \tag{1}$$

$$K^0_S \to \pi^+\pi^-, \tag{2}$$

$$\Lambda \to p\pi^-, \tag{3}$$

where p_s stands for spectator proton. In cases where more than one "neutral" event pointed to a primary vertex, SQUAW also attempted the following fits:

$\pi^0 \to \gamma\gamma$,

$\eta^0 \to \gamma\gamma$,

$\Sigma^0 \to \Lambda\gamma$.

The three-constraint probability distribution from a preliminary sample of unique γ fits was found to be biased toward high probability. This was not true of the unique Λ, K^0 fits. It was discovered that in reaction (1), the average fitted spectator proton momentum from SQUAW was inordinately large. Therefore, the errors on the spectator momentum were scaled relative to the momentum error of the converted γ,

$$(\Delta p_s)_T = (0.05)\Delta P_\gamma,$$

$$(\Delta p_s)_L = (0.01)\Delta P_\gamma,$$

where T and L refer to transverse and longitudinal components relative to the direction of the γ laboratory momentum. It was found that these estimates for the spectator momentum errors improved the three-constraint probability distribution.

E. Beam momentum

In order to transform variables into the proton-proton center of mass system, the momentum and angles of the beam track have to be known at each primary interaction vertex. However, the event measurements did not, in general, include any track at the primary vertex. Therefore, we measured the beam tracks of 1000 primary vertices with associated three-constraint V^0 fits. These measurements were made on POLLY III with the results

$$p(x=0) = 12.35 \pm 0.40 \text{ GeV}/c,$$

$$\phi(x=0) = 354.73^\circ + (0.0095^\circ/\text{cm})y,$$

$$\lambda(x=0) = -0.025^\circ.$$

The proper values of (p, ϕ, λ) for a beam track at any vertex point (x, y) in the chamber were then obtained by extrapolating the parameters at $x=0$ to the point (x, y) using the known energy loss of protons in hydrogen and the curvature produced by the magnetic field.

IV. EVENT SELECTION AND WEIGHT FACTORS

Of the 9718 reconstructed V^0's, we obtained 5979 three-constraint (3C) fits corresponding to a total of 5199 unique and 381 ambiguous 3C V^0's. This amounts to an ambiguity of 6.8%. The remaining 4138 "neutral" events with a 1C fit or no fit at all are those not associated with a reconstructed primary interaction within the chosen fiducial volume. Most of these were produced upstream of the chamber, in the beam window, or in the chamber walls.

A. Separation of the V^0 events into γ's, K_S^0's, and Λ's

The headings of Table I indicates the types of ambiguities encountered between the Λ, K^0, and γ fits. The transverse momentum distribution of the negative track from the neutral events was used to assign ambiguous events to definite channels. An event fitting the Λ (K^0) but also fitting γ was assigned to the γ channel if $P_T^{e^-} < 0.01$ GeV/c (0.02 GeV/c). An event fitting both the Λ and K^0 hypotheses was assigned to the Λ channel if $P_T^{(\pi^-)}(K^0) < 0.11$ GeV/c.

To estimate the losses of Λ's or K_S^0's into the γ sample caused by these assignments, we make use of the fact that the decay of a V^0 in its own rest frame gives a probability distribution for P_T of

$$N(P_T)\,dP_T = \frac{P_T}{P^*}\,\frac{dP_T}{(P^{*2} - P_T^{\,2})^{1/2}}, \quad 0 \le P_T \le P^*$$

where $N(P_T)$ is the fraction of the total number of events expected between P_T and $P_T + dP_T$, and P^* is the particle momentum from the V^0 decay ($P^* = 0.1004$ GeV/c for Λ and 0.206 GeV/c for K_S^0) in the V^0 rest frame. By integrating the above ex-

TABLE I. Classification of 3C fits.

	Unique fits			Ambiguous fits				
	Λ	K^0	γ	$\Lambda\gamma$	ΛK^0	γK^0	$\gamma K^0\Lambda$	Total
Raw number of 3C fits	309	246	4644	173	126	64	18	5580
Selected number of 3C fits								
For Λ	309	...	...	45	123	...	9	486
For K^0	...	246	...	...	3	3	3	255
For γ	...	...	4644	128	...	61	6	4839

pression from 0.0 to 0.01, we find that 0.5% of all Λ's should lie in the region which was assigned to γ's. In Fig. 2(a) we show the $P_T^{\pi^-}$ distribution for all 3C Λ fits inside the fiducial volume. Note that from this event sample, we expect two events in the region of $0.0 \leq P_T^{\pi^-} \leq 0.01$, compared to the one event actually found. Similarly, we integrate from 0.0 to 0.02 for K_S^0's and find that 0.5% should fall in this region. From Fig. 2(b) we estimate that we should have one event instead of zero observed. For the Λ/K^0 ambiguity, we integrate from 0.0 to 0.11 for the K^0 distribution. This yields that 15.5% (i.e., 38 events) of all selected K^0's should be in this interval; instead we find 30. Thus, in all three cases, we have agreement between the number of events expected and those found.

The transverse momentum distribution of the e^- from the γ conversion is sharply peaked at zero with only 27 events having $P_T^{e^-} > 0.02$ GeV/c. Of these, five are unique γ events and the rest are assigned to the Λ or K^0 samples according to the P_T cuts described above. The numbers of selected events are tabulated in Table I.

B. Fiducial volume and minimum length cut

In order to guarantee that all beam tracks had entered the chamber through the beam window, the z and y coordinates of the primary vertex were required to be within $123.5 \text{ cm} \leq z \leq 137.5$ cm, $-110.0 \text{ cm} \leq y \leq 90.0$ cm. For the x coordinate, we chose $-136.0 \leq x \leq 132.0$ cm for the primary vertices associated with the Λ and K^0 events and $-132.0 \leq x \leq 94.0$ cm for those associated with the γ events. This tighter x cut for the γ events was necessary in order to ensure sufficient conversion length for the γ's and thereby avoid large weight factors.[3]

The fiducial volume for the secondary interaction (V^0's) was kept the same for both event samples. It was chosen as a cylinder situated at the center of the chamber with radius $R = 170.0$ cm and with $80.0 \text{ cm} \leq z \leq 190.0$ cm. Note that the bottom of this cylinder is on the average 30 cm from the bottom of the chamber.

In order to check for a possible loss of V^0's close to the primary vertex, we plot in Figs. 3(a) and 3(b) the number of Λ's or K_S^0's versus the decay length L. From these graphs, it is evident that losses occur for Λ's of decay length less than 4 cm and for K_S^0's of length less than 3 cm. These values were chosen as the minimum length cut, $L_{\min}$.

To correct for these $L_{\min}$ cuts, as well as for decays outside the fiducial volume, each Λ or K_S^0 was given the standard weight

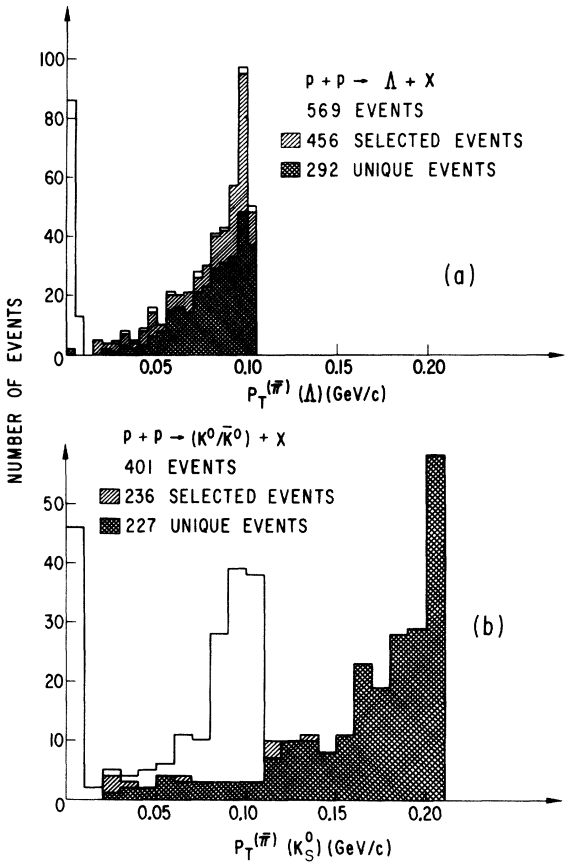

FIG. 2. (a) Transverse momentum distribution of the π^- from Λ decays $[P_T^{(\pi^-)}(\Lambda)]$ for 3-constraint fits inside the fiducial volume. Shaded events are those selected by the $P_T^{(\pi^-)}$ cut. Cross-hatched events are unique fits. (b) Same as (a) for $P_T^{(\pi^-)}(K_S^0)$.

$$W_1 = 1.0/(e^{-L_{\min}/L_0} - e^{-L_{\text{pot}}/L_0}), \tag{4}$$

where L_{pot} is the potential path along the line of flight of a neutral particle (Λ or K_S^0) from the production vertex to the boundary of the fiducial volume, $L_0 = (p/m)c\tau$ with p, m, and τ as the measured momentum, the mass, and the lifetime of the V^0, respectively.

For the γ sample, L_0 in Eq. (4) is the mean conversion length at a given laboratory momentum and is calculated from the pair production cross section given by Knasel.[6] Event losses are clearly visible up to an observed conversion length of 10 cm as shown in Fig. 3(c). To study this loss, we have plotted in Fig. 3(d) the weighted number of γ events as a function of the minimum conversion length accepted ($L_{\min}$). A loss of events is evident for the lower edge at <12 cm, the value chosen for $L_{\min}$. The number of events remaining after the fiducial volume and $L_{\min}$ cuts are listed in Table II.

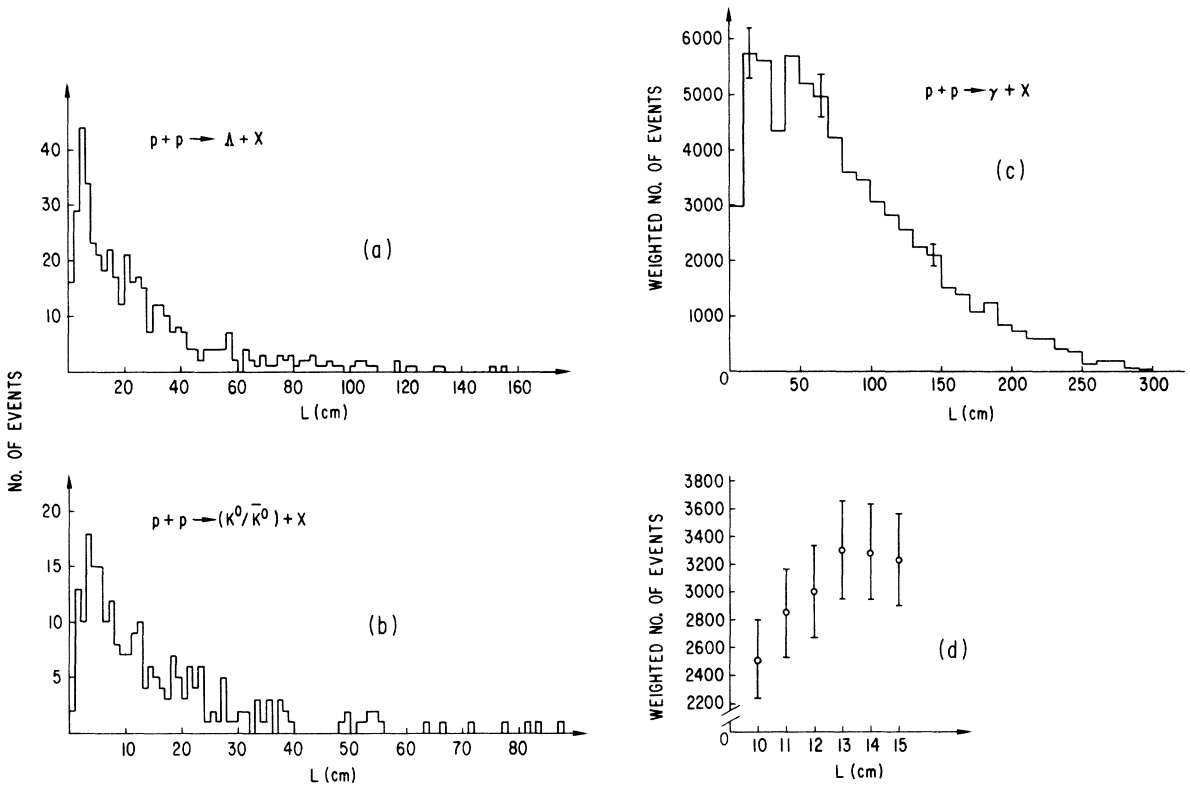

FIG. 3. (a) Length distribution of the Λ events inside the fiducial volume. (b) Length distribution of the K^0 events inside the fiducial volume. (c) Length distribution of γ events inside the fiducial volume. (d) Weighted length distribution of γ events within a 5 cm bin.

C. Scanning efficiency correction factor and cross section normalization

Of the 14 rolls (26 300 frames) analyzed in this experiment, ten rolls (19 100 frames) were double-scanned. For the Λ and K^0_S events, the single-scanning efficiency is $(93 \pm 2)\%$, whereas the double-scanning efficiency is $(99 \pm 1)\%$. For the γ's the data were divided into six equal bins of the center of mass production angle, $\cos\theta^*$, and the scanning efficiency was computed for each bin. The results are shown in Table III. The scanning efficiency correction factor, W_2, for all events is then calculated for the single- and double-scanned events as appropriate.

The cross section normalization was determined from a beam track count in every tenth frame. We find for the γ events a value of 1.05 ± 0.05 events/μb, whereas for the Λ and K^0_S events, because of the larger fiducial volume, this number is 1.21 ± 0.06 events/μb. The corresponding factor, W_3, is the inverse of these values [Table II].

D. Center-of-mass symmetry corrections

In order to check for further event losses, we plotted in Fig. 4(a) the production angle of the Λ's in the pp center-of-mass system. It is evident

TABLE II. Number of events after various cuts.

Event type	After fiducial volume and length cuts	After forward-backward symmetry cuts	Average weight [a]	μb/Event	Correction for unreconstructed events
Λ	411	411	1.52	$1.0/(1.21 \pm 0.06)$	1.33 ± 0.09
K^0_S	211	204	1.67	$1.0/(1.21 \pm 0.06)$	1.62 ± 0.16
γ	3752	3587	14.54	$1.0/(1.05 \pm 0.05)$	1.27 ± 0.13

[a] For further details, see Sec. IV.

from this plot that the departure from the expected forward-backward symmetry suggests event losses for $\cos\theta^* > 0.85$, i.e., very forward events. The ratio of weighted events in the forward hemisphere to those in the backward hemisphere is equal to 0.78 ± 0.08, which indicates, assuming that all backward events are seen, that 22% of the forward hemisphere events are lost (58 unweighted events). To check whether these losses might be due to $\Lambda + p$ interactions, we weight each event by the inverse of the interaction probability using $\sigma(\Lambda p) = 35$ mb (see Ref. 7) and find that this accounts for only 4% of the 22% loss.[8] To correct our cross sections for the forward Λ losses, we have scaled the three forward-most bins in $\cos\theta^*$ [Fig. 4(a)] by the backward-to-forward ratio for each bin separately.

TABLE III. Scanning efficiencies for γ events.

$\cos\theta^*$	Scan 1	Scan 2	Both scans
$-1.0 \rightarrow -0.667$	0.78 ± 0.11	0.66 ± 0.11	0.93 ± 0.05
$-0.667 \rightarrow -0.333$	0.86 ± 0.07	0.78 ± 0.07	0.97 ± 0.02
$-0.333 \rightarrow 0.0$	0.82 ± 0.07	0.77 ± 0.07	0.96 ± 0.02
$0.0 \rightarrow +0.333$	0.85 ± 0.07	0.82 ± 0.07	0.97 ± 0.02
$0.333 \rightarrow +0.667$	0.88 ± 0.05	0.83 ± 0.05	0.98 ± 0.01
$0.667 \rightarrow 1.0$	0.88 ± 0.04	0.78 ± 0.04	0.98 ± 0.01

Turning now to the K^0_S events, we note that after

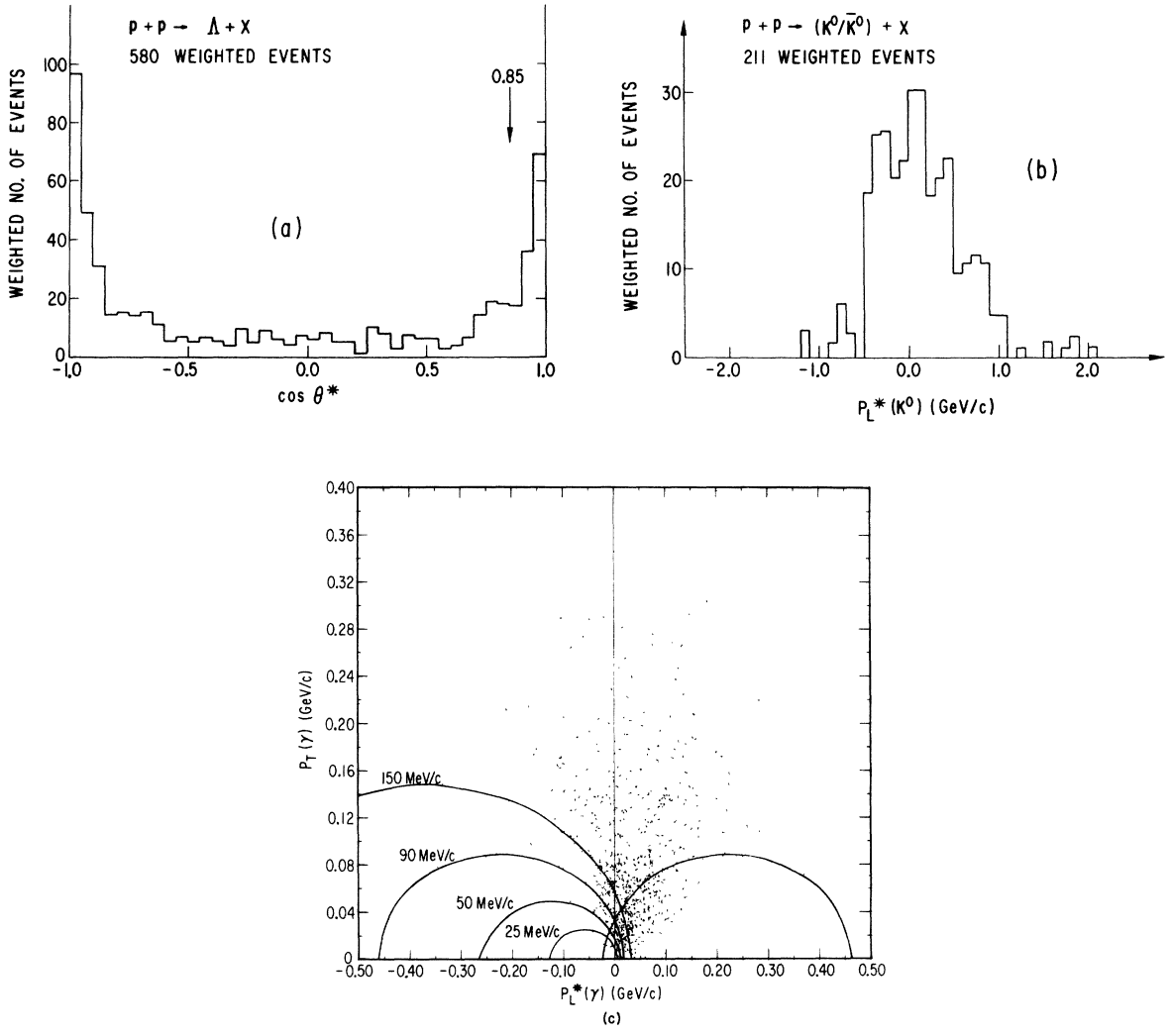

FIG. 4. (a) $\cos\theta^*$ of Λ's in the over-all center-of-mass system. Events are inside the fiducial volume and have a length $L > 4.0$ cm. (b) Histogram of P^*_L for weighted K^0_S events. Events are inside fiducial volume and have a length $L > 3.0$ cm. (c) Peyrou (P_T versus P^*_L) plot of unweighted γ events inside fiducial volume and with length $L > 12.0$ cm. The curves in the backward hemisphere correspond to $P^{\gamma}_{\text{lab}} = 25$, 50, 90, and 150 MeV/$c$. The corresponding reflected curve for 90 MeV/c is shown in the forward hemisphere.

the fiducial volume and length cuts, we are left with 211 events [Table II]. Their backward-to-forward ratio is 0.69 ± 0.10, which indicates a loss of 31% of the events in the backward c.m. hemisphere (22 unweighted events). From the weighted histogram of P_L^* shown in Fig. 4(b), we clearly see the loss of events in the backward hemisphere for $P_L^* < -0.5$ GeV/c. We do not have any clear explanation for these losses. One can argue, however, that these are low P_{lab}, high P_T events produced at large angles ($> 45°$) with respect to the beam direction in the laboratory, and thus would be susceptible to a severe scanning loss. In order to correct for these losses, we remove the 7 events with $P_L^* < -0.5$ GeV/c and weight those with $P_L^* > 0.5$ GeV/c by a factor of 2.

For the γ's, we are left with 3752 events after fiducial volume and length cuts. To check for forward-backward symmetry, we display in Fig. 4(c) a Peyrou plot of P_T versus P_L^* in the over-all center-of-mass system. The curves in the backward hemisphere represent constant laboratory momenta of 25, 50, 90, and 150 MeV/c. The plot clearly indicates a loss of events for low laboratory momenta. To determine the extent of these losses, we have deleted events with less than a particular P_{lab}, as well as those that lie under the reflected curve in the forward hemisphere. For the remaining events, we then plot in Fig. 5 the backward to forward ratio using weighted events as a function of the P_{lab} cut for all events and separately for three intervals in $|\cos\theta^*|$. It is clear that there are losses for $P_{\text{lab}}^{\gamma} < 90.0$ MeV/c except for $-0.33 < \cos\theta^* \leq 0.0$. In region $-1.0 < \cos\theta^* \leq -0.67$, there is an additional loss of about 4% of the total γ cross section that is not a function of P_{lab}. Since the correction for unreconstructed events is large (see section below), to avoid the possibility of double weighting we have not applied an additional correction in this kinematic region. Thus, we remove all events with $P_{\text{lab}}^{\gamma} < 90.0$ MeV/c and $P_L^* < 0.0$. Events in the forward hemisphere under the reflected curve are then weighted by a factor of 2. Note that the 90 MeV/c curve extends slightly into the forward hemisphere and events observed in this region are also weighted by 2. There may remain a loss of very low momentum γ's in this region. This loss is estimated from phase space considerations to be small and is therefore neglected. The final numbers of events after all these cuts are listed in Table II. The corresponding center-of-mass system symmetry correction is called W_4.

E. Unreconstructed event correction factor

Another large correction factor is contributed by the unreconstructed events. In order to determine this factor, physicists examined unreconstructed events found on 4 out of the 14 rolls employed. The study involved about 1000 V^0 candidates. By insisting that these V^0's (1) be associated with a primary vertex, (2) be within the fiducial volume, and (3) definitely resemble γ, K^0, or Λ, approximately 600 events were retained as good V^0 candidates. After careful examination, these 600 events were taken as a representative sample of all scanned events and the correction factors obtained from these V^0's were applied to the total sample. Since there was no obvious reason why these V^0's differ from the well-reconstructed events, we assumed that the fraction pointing back to a primary vertex is the same for both samples. From these ratios, one then obtains the over-all correction factor (W_5) for event losses due to unreconstructed events: 1.33 ± 0.09 and 1.62 ± 0.16 for the Λ and K_S^0 samples, respectively. Because of the larger statistics in the γ sample, this correction factor was calculated independently for each topology. Within errors, they are equal to the average of 1.27 ± 0.13. More detailed discussion of these corrections can be found in Ref. 3.

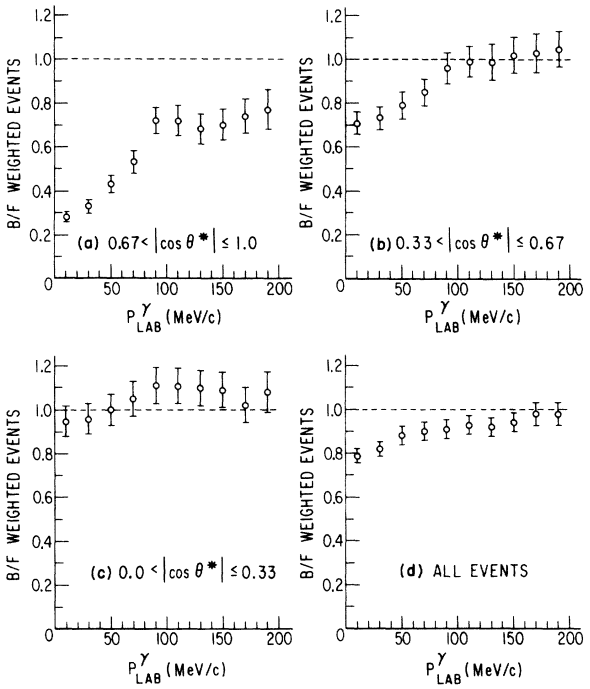

FIG. 5. Backward to forward ratios of weighted γ events as a function of P_{lab}^{γ}. In each case, events with momentum less than P_{lab}^{γ} as well as those under the reflected curve in the forward hemisphere have been removed. (a) Events which satisfy $1.0 < |\cos\theta^*| \leq 0.67$. (b) Events which satisfy $0.67 < |\cos\theta^*| \leq 0.33$. (c) Events which satisfy $0.33 < |\cos\theta^*| \leq 0$. (d) All events.

F. The χ^2 probability cut and correction factor

The χ^2 probability distributions for the Λ, K^0_S, and γ events are shown in Fig. 6. In all distributions, there is an excess of events with $P(\chi^2)<1\%$. No correlation was found between these low probability events and other variables such as decay or conversion lengths, P_{lab}, and the azimuthal production angle in the laboratory frame, etc. Therefore, we include all events for cross section purposes. However, for detailed analysis in terms of any kinematic variable, we excluded from our samples all events with $P(\chi^2)<1\%$ and normalized all distributions to the total cross sections. This correction factor (W_6) equals 1.12, 1.08, and 1.07 for the Λ, K^0_S, and γ events, respectively.

In the previous sections, we have described six correction factors employed in this experiment. Their product gives then the total weight factor for each event.

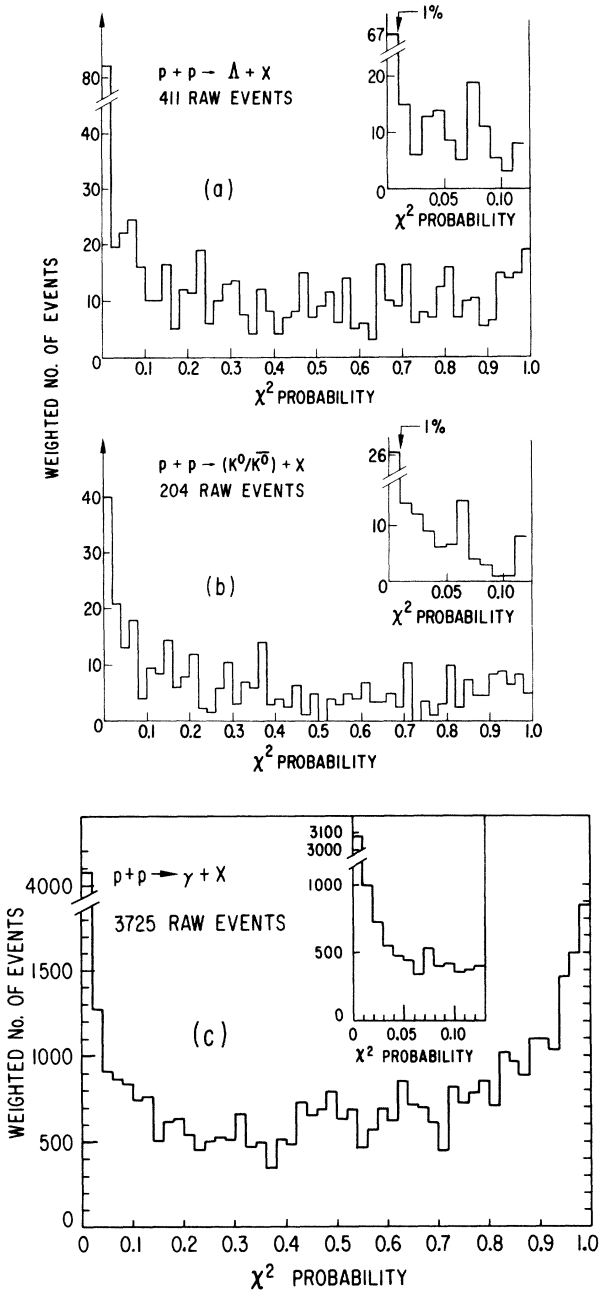

FIG. 6. (a) χ^2 probability distribution for Λ events (insert: expanded scale for low probability events). (b) Same as (a) for $K^0/\bar{K}^0$ events. (c) Same as (a) for γ events.

V. MASS OF K^0 AND Λ AND CROSS SECTIONS

A. Mass of K^0 and Λ

As described in the previous section, the final selected number of K^0_S's (Λ's) events is 204 (411). To check the magnetic field map as well as the accuracy of the bubble chamber reconstruction, we plotted Gaussian ideograms and histograms of the measured mass values. These graphs yielded

$$M(K^0) = 497.8 \pm 0.3 \text{ MeV}/c^2,$$

with a half width at half maximum of 5 MeV/c^2 and

$$M(\Lambda) = 1115.6 \pm 0.1 \text{ GeV}/c^2,$$

with a half width at half maximum of 1.5 MeV/c^2. Both values are in agreement with the world averages of 497.70 ±0.13 MeV/c^2 and 1115.60 ±0.05 MeV/c^2, respectively.[9]

B. Cross sections from multiple V^0 events

In order to obtain cross sections for π^0, η, and Σ^0 production, we formed the invariant $\gamma\gamma$, $\Lambda\gamma$, and ΛK^0 mass distributions for double V^0 events (Tables IV and V) for which both V^0's are associated with the same pp interaction. As discussed in Ref. 2, the 111 events which fit $\pi^0 \to \gamma\gamma$ yield an

TABLE IV. Number of multiple γ events.[a]

Topology	$p+p \to$ $1\gamma+X$	$2\gamma+X$	$3\gamma+X$	$4\gamma+X$
2 prongs	1040(21.15)	104(18.57)	10(16.68)	•••
4 prongs	1266(19.41)	141(19.45)	7(15.07)	1(13.14)
6 prongs	380(19.67)	37(17.90)	3(24.85)	•••
8 prongs	48(18.10)	6(11.61)	•••	•••
10 prongs	1(11.55)	•••	•••	•••

[a] Numbers in parentheses represent the average weight per γ for the respective channel only.

inclusive π^0 cross section

$$\sigma(p+p \to \pi^0_{\searrow\gamma\gamma} + X) = 33.1 \pm 5.6 \text{ mb}.$$

Since no η signal is observed in the $\gamma\gamma$ mass distribution of Fig. 7(a), an upper limit can be set,

$$\sigma(p+p \to \eta_{\searrow\gamma\gamma} + X) \leq 0.5 \text{ mb} \quad (95\% \text{ confidence level}).$$

The $\Lambda\gamma$ mass distribution [Fig. 7(b)] shows a small Σ^0 enhancement above a background. Five of the events yielded a Σ^0 fit indicated in Fig. 7(b). By

TABLE V. Number of multiple V^0 events.

$p+p \to$	Number of events[a]
$\gamma+\Lambda+X$	79(20.09)
$\gamma+K^0_S+X$	24(23.38)
$\Lambda+\Lambda+X$	1(1.40)
$\Lambda+K^0_S+X$	19(2.00)
$K^0_s+K^0_S+X$	4(2.43)

[a] Numbers in parentheses represent the average of the product of the two weights $\langle W_1 \cdot W_2 \rangle$.

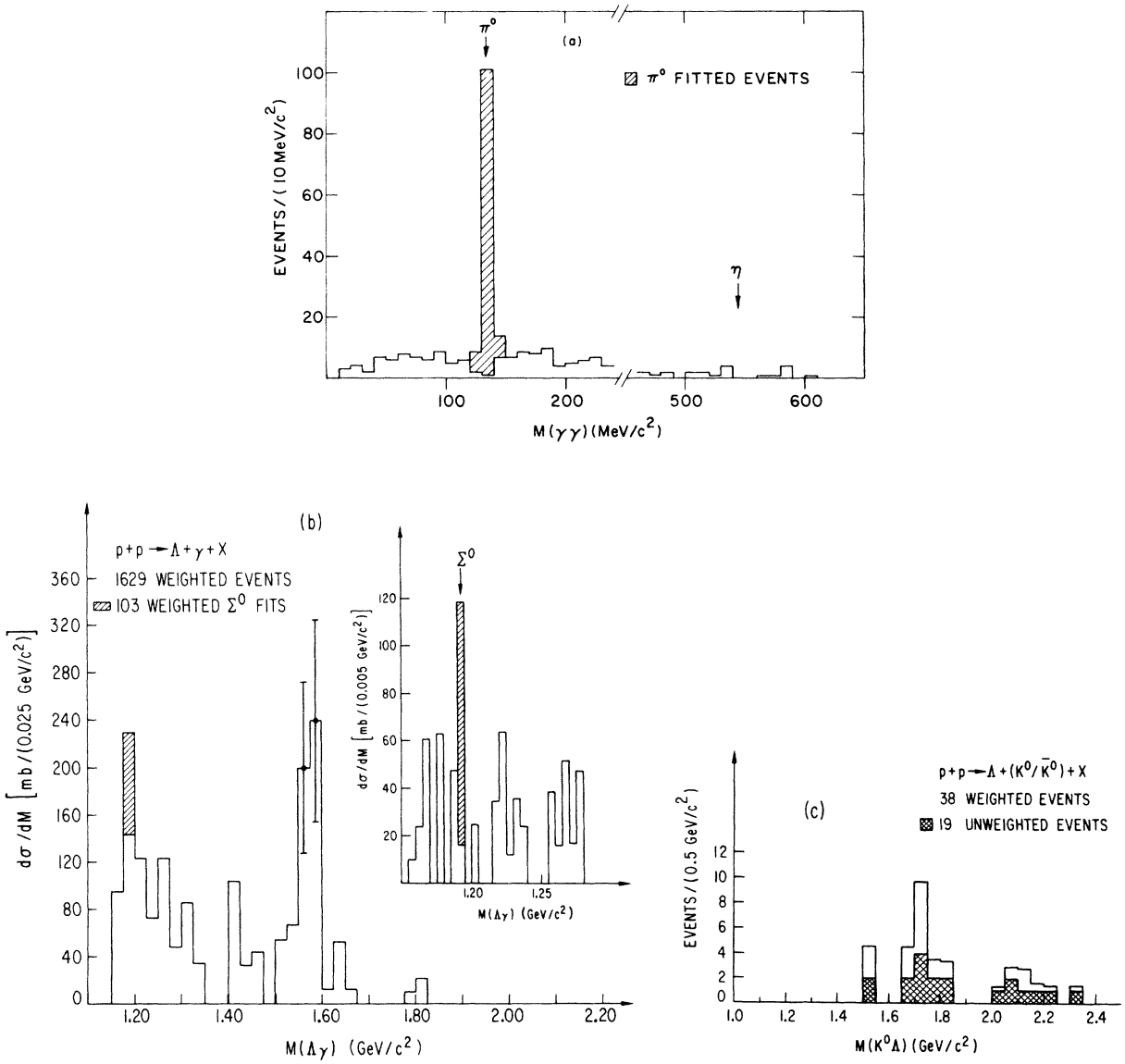

FIG. 7. (a) $\gamma\gamma$ mass distribution (unweighted events). Shaded events represent fits to $\pi^0 \to \gamma+\gamma$. (b) $\Lambda\gamma$ mass distribution (cross section equivalent weights). The insert shows the $\Lambda\gamma$ mass region between 1.15 and 1.28 GeV/c^2. Shaded events represent fits to $\Sigma^0 \to \Lambda+\gamma$. (c) ΛK^0_s mass distribution (weighted events). Shaded events represent the unweighted events.

using these five fits, we obtain a cross section of

$$\sigma(p+p \to \Sigma^0_{\searrow \Lambda\gamma}+X) = 103 \pm 47\ \mu\text{b},$$

a result which agrees with the value obtained by estimating a Σ^0 signal above a small background.[10] The insert in Fig. 7(b) shows the Σ^0 mass region in more detail on an expanded scale.

The mass enhancement at $M(\Lambda\gamma) \cong 1.575$ GeV/c^2 corresponds to a 3 standard deviation effect and has a full width at half maximum of ~50 MeV/c^2. Since the effective masses of $M(\Lambda\gamma)$ from Σ^* resonances of mass greater or equal to 1.765 GeV/c^2, i.e., $\Sigma^* \to \Lambda\pi^0$ with the $\pi^0 \to \gamma\gamma$, reflect into this mass region, no further conclusion on this mass bump can be drawn at this time. The ΛK^0_S mass distribution [Fig. 7(c)] yields no substantial information on the ΛK^0 decay mode of N^* states.

In Table IV we have listed the number of 1γ, 2γ, 3γ, and 4γ events as a function of topology. Also indicated are the average weights per gamma in each channel. The number of multiple V^0 events are listed in Table V. The total weight for each of these events is the product of the individual weights. The averages of these products in each channel are also listed.

C. Total and topological cross sections

In Table VI we list the number of raw events as a function of topology together with the corresponding cross sections. For the Λ and K^0 events, we have corrected for unseen decay modes.[9] The total inclusive cross sections are

$$\sigma(p+p \to \Lambda + X) = 1.07 \pm 0.11 \text{ mb},$$

$$\sigma(p+p \to K^0/\bar{K}^0 + X) = 1.37 \pm 0.16 \text{ mb},$$

$$\sigma(p+p \to \gamma + X) = 63.1 \pm 5.1 \text{ mb}.$$

The most likely sources of γ's other than from π^0 decays are η and Σ^0 decays. From the inclusive η and Σ^0 cross sections quoted above, we see that they contribute $\lesssim 1$ mb to the inclusive γ cross section. Neglecting these, thereby assuming that all γ's originate from π^0 decays, yields

$$\sigma(p+p \to \pi^0 + X) = 31.6 \pm 2.6 \text{ mb}.$$

Since this value agrees with the direct measurements quoted above from a small sample of $\pi^0 \to \gamma\gamma$ events, we conclude that it is our best estimate for the inclusive π^0 cross section, and that π^0 decay is the source of at least 98% of the photons we observe. The inclusive π^0 cross section is plotted in Fig. 8 together with data at other momenta.[11-17] The topological π^0 cross sections are also presented in Table VI.

VI. MULTIPLICITIES OF THE INCLUSIVE π^0, K^0, Λ EVENTS

From the topological cross sections listed in Table VI, we calculate the average number of $\langle\Lambda\rangle$, $\langle K^0/\bar{K}^0\rangle$, and $\langle\pi^0\rangle$ per inelastic pp collision

$$\langle V^0\rangle_n = \sigma_n(V^0)/\sigma_n(pp),$$

where the inelastic topological pp cross sections at 12.0 GeV/c are given by Ref. 11 and n is the number of charged particles produced. The results are in Table VII and are plotted in Fig. 9, which also includes data from the 19.0 GeV/c (see Ref. 12) and 69.0 GeV/c (see Ref. 13) pp experiments for the Λ and K^0. The $\langle\pi^0\rangle$ values are compared with data from the 69.0 GeV/c (see Ref. 13) and 102.0 GeV/c (see Ref. 14) experiments. In all three cases, the $\langle V^0\rangle_n$ becomes more positive as the energy increases. Furthermore, at a given energy, the $\langle V^0\rangle_n$ becomes more positive as the mass of the V^0 decreases.

We have also plotted the average value $\langle\pi^0\rangle = 1.06 \pm 0.09$ together with other data[11-18] as a function of s, the total center of mass energy squared (Fig. 10). The straight line represents a fit of the form[19]

$$\langle\pi^0\rangle = -(1.68 \pm 0.19) + (0.87 \pm 0.05)\ln s.$$

TABLE VI. Inclusive total and topological cross sections for $p+p \to (\Lambda, K^0, \gamma)+X$.

Topology	Λ events Raw no. of events	$\sigma(pp \to \Lambda+X)$ [a] (mb)	K^0 events Raw no. of events	$\sigma(pp \to K^0/\bar{K}^0+X)$ [a] (mb)	γ events Raw no. of events	$\sigma(pp \to \gamma+X)$ [a] (mb)	$\sigma(pp \to \pi^0+X)$ [a] (mb)
2	237	0.650 ± 0.092	101	0.690 ± 0.120	1349	25.0 ± 2.2	12.5 ± 1.1
4	148	0.359 ± 0.053	87	0.573 ± 0.103	1678	28.6 ± 2.4	14.3 ± 1.2
6	24	0.056 ± 0.013	15	0.103 ± 0.031	496	8.5 ± 0.8	4.25 ± 0.4
8	2	0.004 ± 0.003	1	0.005 ± 0.005	63	0.94 ± 0.16	0.47 ± 0.08
10	...	...	...	...	1	0.01 ± 0.01	0.005 ± 0.005
Total	411	1.069 ± 0.107	204	1.371 ± 0.161	3587	63.1 ± 5.1	31.6 ± 2.6

[a] All errors include an 8% systematic uncertainty.

In order to present similarities between the charged multiplicities for all events and for those associated with π^0, K^0, and Λ production, we have calculated the quantities

$$\langle n_{ch}\rangle^k = \frac{\sum n\sigma_n^k}{\sigma_{total}^k},$$

where k stands for π^0, K^0, and Λ associated events, and n is the number of charged particles at the primary vertex. For the total charge multiplicities, we use

$$\langle n_{ch}\rangle = \frac{\sum n\sigma_n}{\sigma_{pp(\text{inelastic})}}.$$

The values so obtained are graphed in Fig. 11 as a function of s.[20] It is quite apparent that all values are consistent with the same curve. Using all data points shown, we obtained the fit shown on the graph

$$\langle n_{ch}\rangle^{all} = -(1.69\pm0.08) + (1.56\pm0.02)\ln s.$$

To demonstrate the nearly equal values of $\langle n_{ch}\rangle^{\pi^0}$ and $\langle n_{ch}\rangle$ even further, we plotted the ratio of these two values as a function of s, shown in the insert of Fig. 11. It is clear that the ratio stays around unity. Similar results hold for both the K^0 and Λ production data. Thus, over a wide range of s, we observe that the average charge multiplicity in pp interactions is the same whether or not π^0's are produced, and even whether or not neutral strange mesons ($K^0/\bar{K}^0$) or baryons (Λ/Σ^0) are also created in the interaction.

VII. DIFFERENTIAL CROSS SECTIONS

In this section the data will be discussed in terms of the variables P_T (the transverse momentum) and x (the Feynman scaling variable), defined as $x = P_L^*/P_{max}^*$, where P_L^* = longitudinal momentum in the over-all c.m. and P_{max}^* = maximum c.m. momentum of the particle.[21] The invariant cross section is written as

$$f(x, P_T^2, s) = \frac{E^* d^3\sigma}{d\vec{p}^{\,*3}} = \frac{E^*}{\pi P_{max}^*}\frac{d^2\sigma}{dx\,dP_T^2}.$$

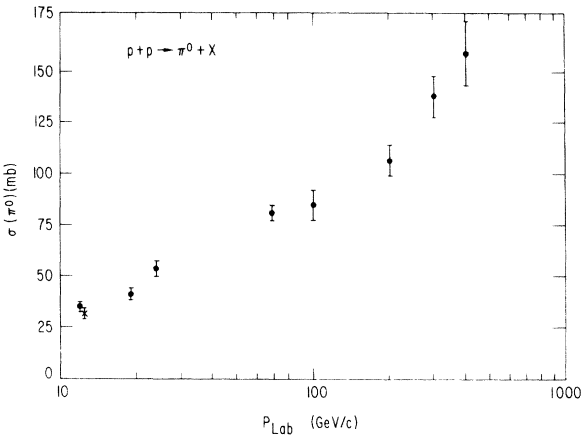

FIG. 8. Inclusive $p+p \to \pi^0 + X$ cross sections. Data from this experiment and from Refs. 11–17.

If Feynman scaling exists, then it is expected that this function will become independent of s (= square of the over-all c.m. energy). Integration over P_T^2 yields

$$F_1(x) = \int \frac{E^*}{\pi P_{max}^*}\frac{d^2\sigma}{dx\,dP_T^2}\,dP_T^2.$$

Because of the limited statistics, we have folded the forward and backward events with respect to $x = 0$ and added the distributions. In Fig. 12 we present the $d\sigma/d|x|$ as well as the $F_1(|x|)$ distributions for the Λ data. Similarly, the K^0 values are plotted in Fig. 13. The difference in shape between the two graphs is evident. While the K^0's are mainly produced in the central region $|x| \lesssim 0.4$, the Λ's are produced up to $|x| = 0.8$.

In Figs. 14(a) and 14(b), we present the $d\sigma/dP_T^2$ distributions for inclusive Λ and K^0 production, respectively. In both cases, the data agree with those from the 12.0-GeV/c experiment.[11]

The rapidity distributions in the over-all c.m. system are presented in Figs. 15 and 16 for K^0 and Λ, respectively. The variable is defined as

TABLE VII. Average number of Λ, K^0, and π^0 per inelastic pp collision.

No. of prongs	σ_n (pp) [a] (mb)	$\langle\Lambda\rangle$	$\langle K^0/\bar{K}^0\rangle$	$\langle\pi^0\rangle$
2	12.7 ± 0.25	0.051 ± 0.007	0.054 ± 0.009	0.98 ± 0.09
4	13.2 ± 0.10	0.027 ± 0.005	0.043 ± 0.009	1.08 ± 0.09
6	3.45 ± 0.04	0.016 ± 0.004	0.030 ± 0.009	1.25 ± 0.12
8	0.381 ± 0.013	0.011 ± 0.008	0.013 ± 0.013	1.23 ± 0.21
10	0.013 ± 0.002	•••	•••	0.39 ± 0.39
Total	29.75 ± 0.25	0.036 ± 0.004	0.046 ± 0.005	1.06 ± 0.09

[a]Data at 12.0 GeV/c from Ref. 11.

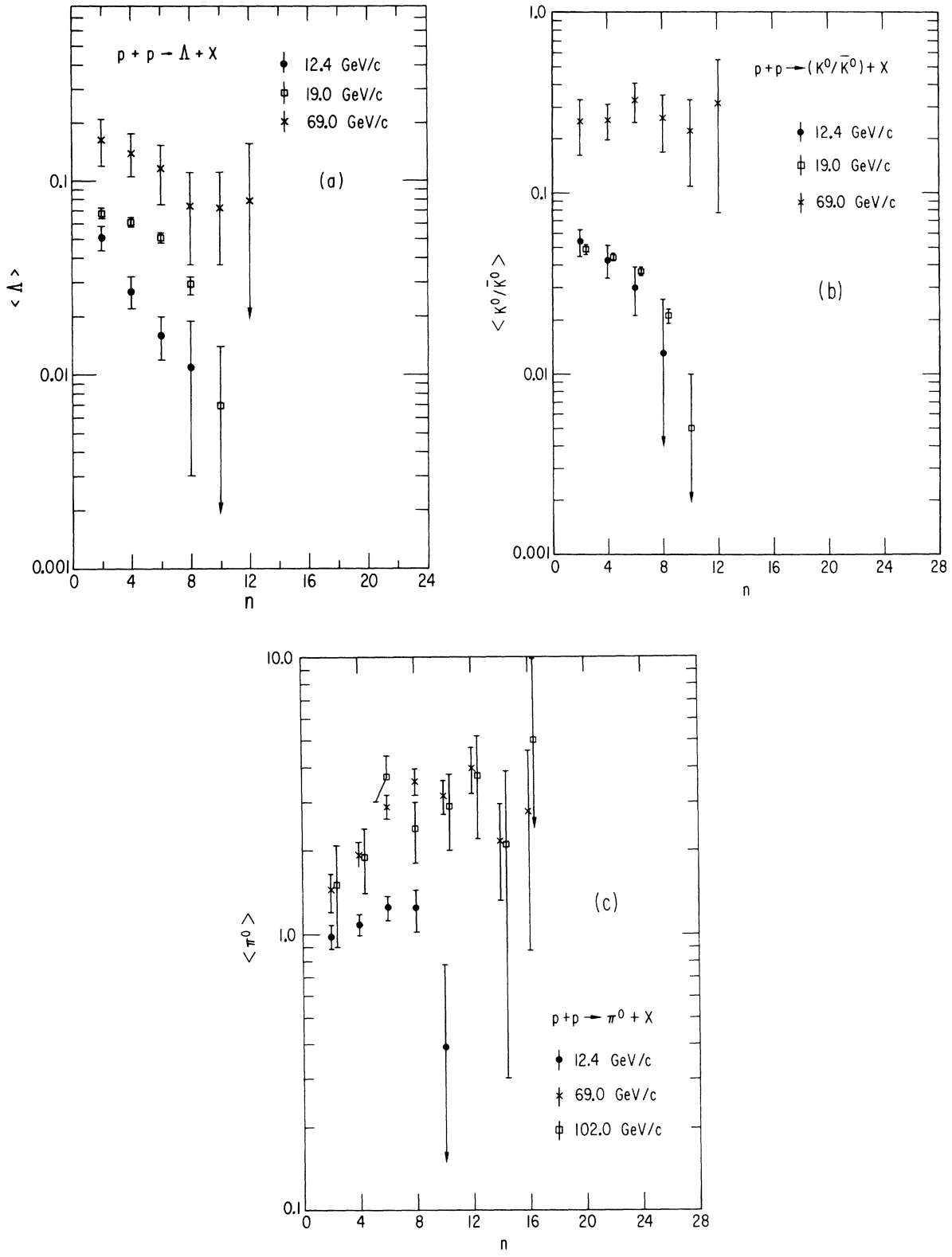

FIG. 9. (a) Average number of Λ, $\langle\Lambda\rangle$, as a function of topology, n, for this experiment and also from Refs. 12 and 13. (b) Same as (a) for $\langle K^0/\bar{K}^0\rangle$; also shown are data from Refs. 12 and 13. (c) Same as (a) for $\langle\pi^0\rangle$; also shown are data from Refs. 13 and 14.

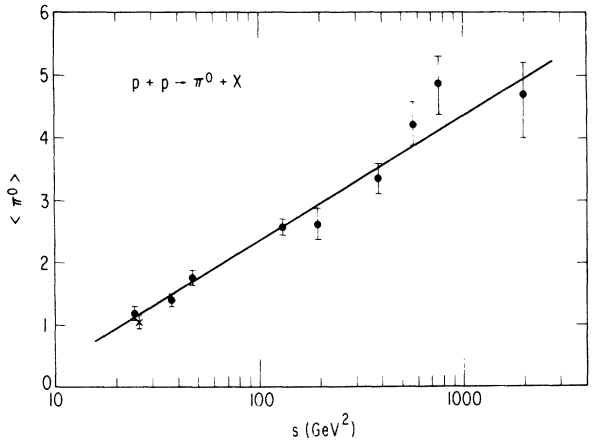

FIG. 10. Total average values, $\langle \pi^0 \rangle$, as a function of s. The straight line is $\langle \pi^0 \rangle = -(1.68 \pm 0.19) + (0.87 \pm 0.05)$ ln$s$.

$$y^* = \frac{1}{2} \ln\left(\frac{E^* + P_L^*}{E^* - P_L^*}\right),$$

with all $*$ quantities referring to the over-all c.m. system. In both graphs, the distribution has been folded about $y^* = 0$ and added. The solid line represents the 19-GeV/c data.[12] Rapidity distributions in the c.m. system for the γ events are plotted in Fig. 17 for all events and for individual charged topologies.

Most of the inclusive γ and π^0 data from this experiment have already been published.[1,2] To derive inclusive π^0 differential cross sections, $g(P^{\pi^0})$, from the inclusive γ spectra, $f(P^{\gamma})$, we use the

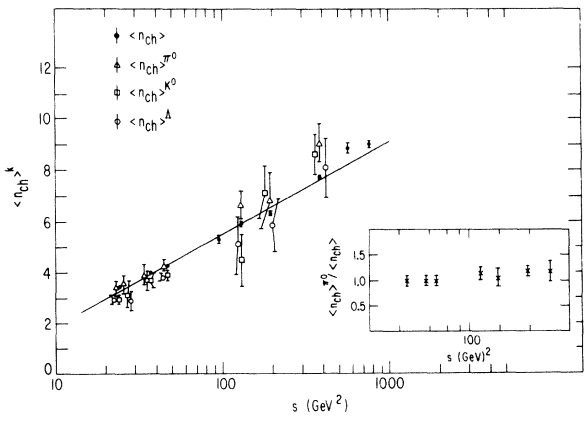

FIG. 11. Average charged multiplicities for all events, and for those events associated with π^0, K^0, Λ production. See text for further details. The curve represents a fit to all data points of the form $\langle n_{ch} \rangle^{all} = -(1.69 \pm 0.08) + (1.56 \pm 0.02)$ ln$s$. The insert to the figure shows the ratio $\langle n_{ch} \rangle^{\pi^0} / \langle n_{ch} \rangle$.

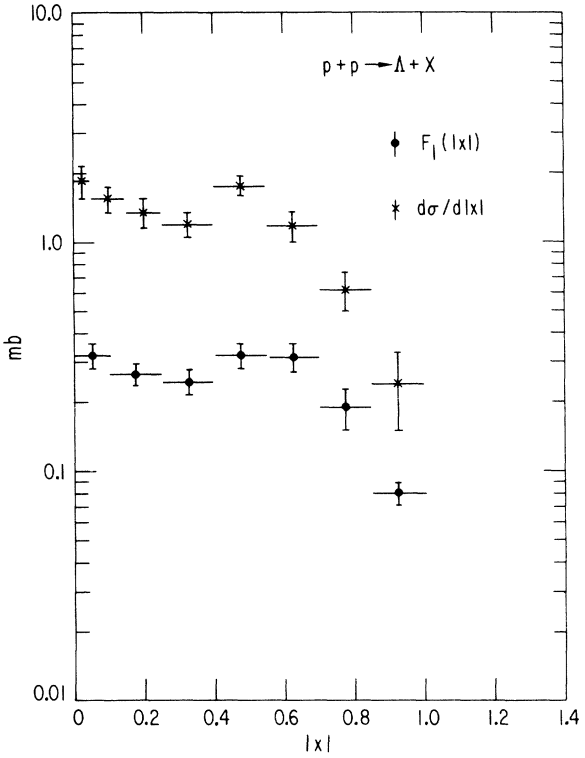

FIG. 12. $d\sigma/d|x|$ and $F_1(|x|)$ for $p + p \to \Lambda + X$. The data have been folded and added about $x = 0$.

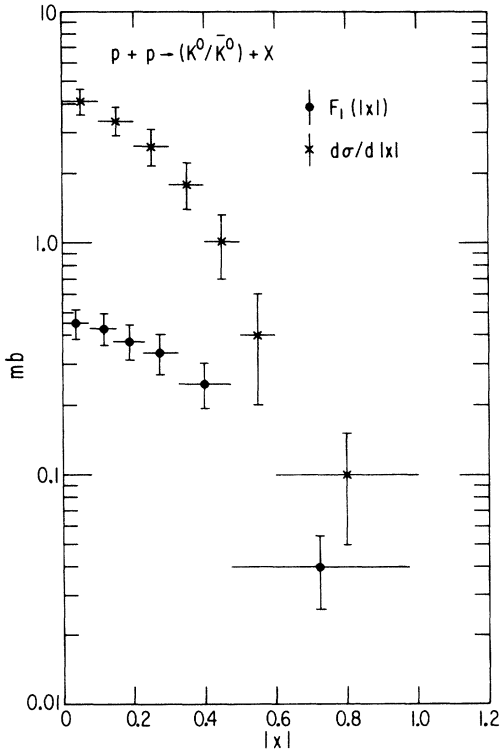

FIG. 13. Same as Fig. 12 for $p + p \to (K^0/\bar{K}^0) + X$.

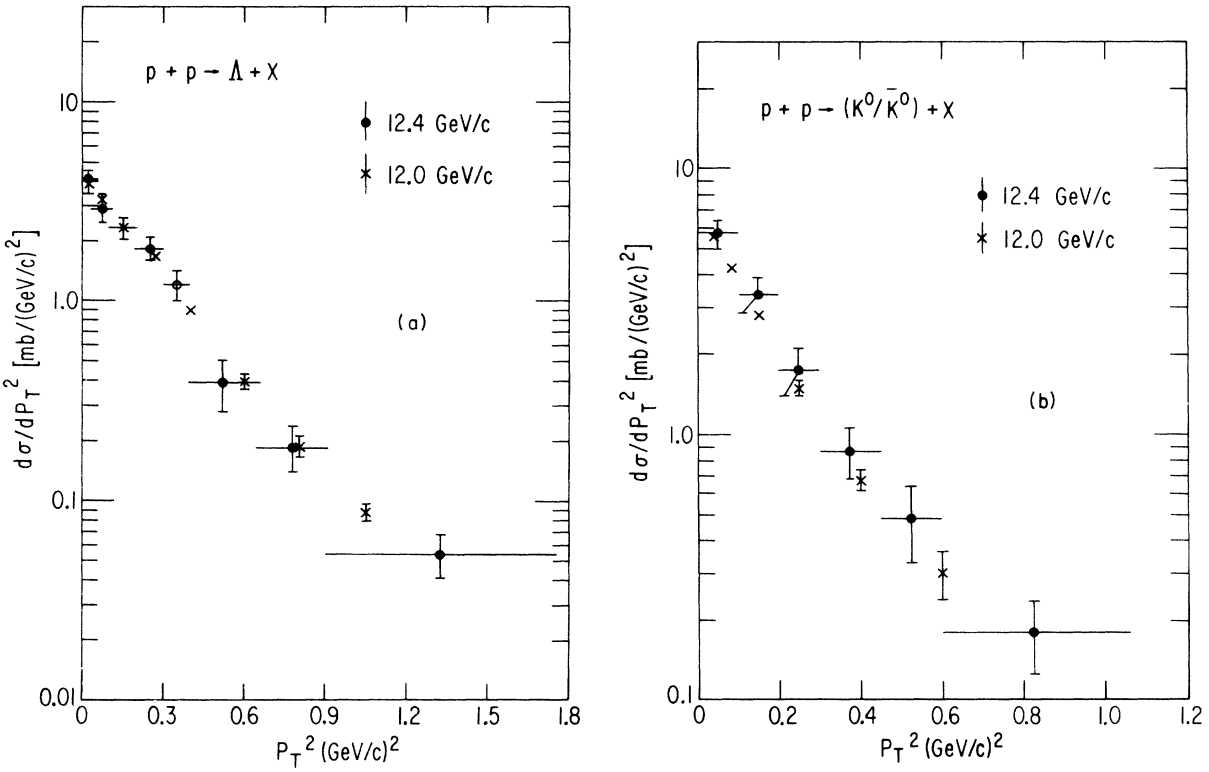

FIG. 14. (a) $d\sigma/dP_T^2$ for $p+p \to \Lambda + X$. Data from Ref. 11 are also shown. (b) Same as (a) for $p+p \to (K^0/\bar{K}^0)+X$.

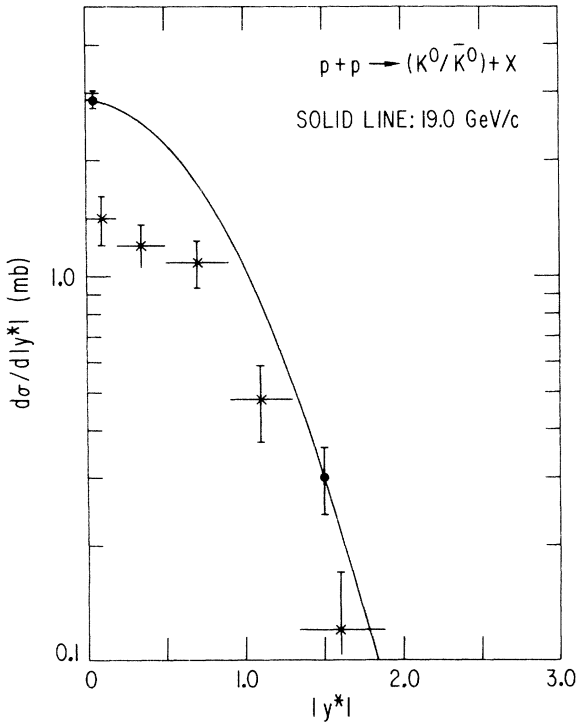

FIG. 15. $d\sigma/dy^*$ for $p+p \to (K^0/\bar{K}^0)+X$. Data from Ref. 12 are also shown. The data have been folded and added about $y^*=0$.

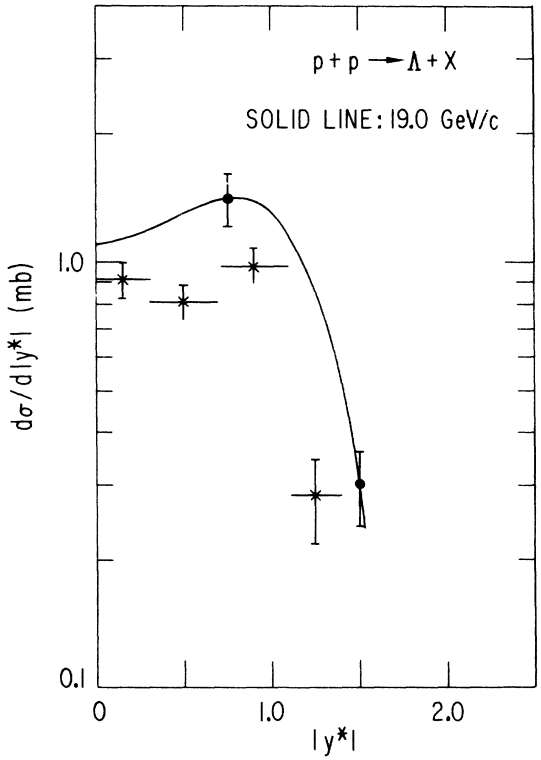

FIG. 16. Same as Fig. 15 for $p+p \to \Lambda + X$.

relation[22]

$$g(P_i^{\pi^0}) = P_i^{\gamma} df/dP_i^{\gamma}|_{P_i^{\gamma}=P'},$$

with

$$P' = \tfrac{1}{2}\{P_i^{\pi^0} + [(P_i^{\pi^0})^2 + (M_{\pi^0})^2]^{1/2}\}. \quad (5)$$

For P_i we choose the longitudinal c.m. component P_L^* or one of the transverse components P_y. In order to carry out the differentiation required, the differential cross section $f(P_L^{*\gamma}) = d\sigma/d|P_L^{*\gamma}|$ [Fig. 18(a)] has been fitted to[23]

$$\frac{d\sigma}{d|P_L^{*\gamma}|} = \sum_{i=1}^{3} A_i \exp[-B_i|P_L^{*\gamma}|],$$

and we obtain $g(P_L^{*\pi^0}) = d\sigma/d|P_L^{*\pi^0}|$ using Eq. (5). This curve is presented in Fig. 18(b) together with data points from our $\pi^0 \to \gamma\gamma$ fits. In a similar manner, the $d\sigma/d|P_y^{\gamma}|$ distribution was fitted to[24]

$$\frac{d\sigma}{d|P_y^{\gamma}|} = \sum_{i=1}^{2} A_i \exp[-B_i|P_y^{\gamma}|],$$

and we obtain $g(P_y^{\pi^0}) = d\sigma/dP_y^{\pi^0}$ using Eq. (5). In order to obtain the transverse momentum distribution, $h(P_T^{\pi^0})$, we calculate[25]

$$h(P_T^{\pi^0}) = -\frac{2}{P_T^{\pi^0}} \frac{d}{dP_T^{\pi^0}} \int_{P_T^{\pi^0}}^{\infty} g(P_y^{\pi^0}) \frac{P_y^{\pi^0} dP_y^{\pi^0}}{(P_y^{\pi^0 2} - P_T^{\pi^0 2})^{1/2}},$$

with the result plotted in Fig. 19.

We observe that the data from the π^0 fits agree well with the transformed γ distributions for all values of $|P_L^{*\pi^0}|$ and $P_T^{*\pi^0}$. Furthermore, these figures include data from the 12.0-GeV/c experi-

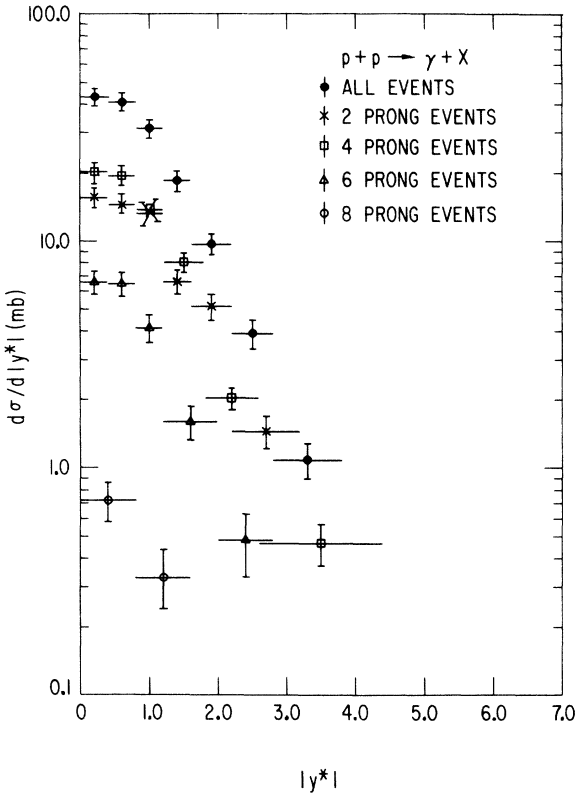

FIG. 17. $d\sigma/d|y^*|$ for the inclusive γ events. The data have been folded and added about $y^*=0$. Data points for 2-, 4-, 6-, 8-prong events are given separately.

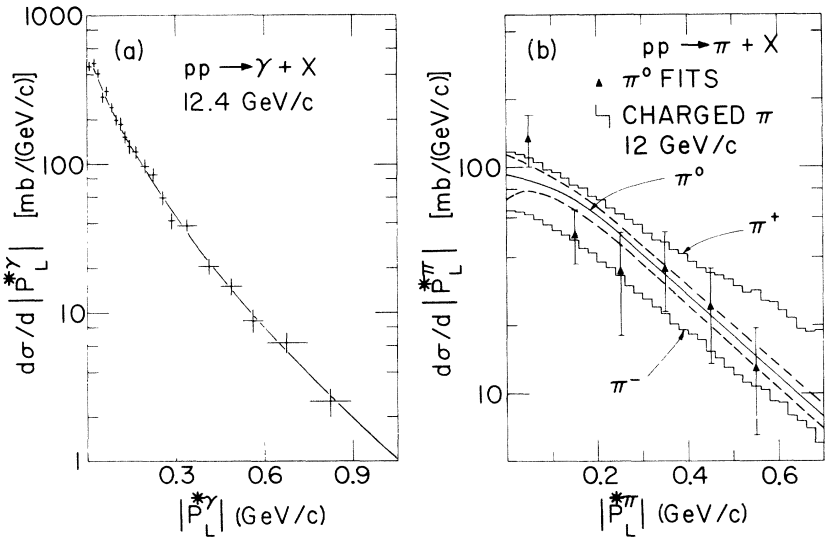

FIG. 18. (a) $d\sigma/d|P_L^{*\gamma}|$ for inclusive γ events. The data have been folded and added about $P_L^{*\gamma}=0.0$. The curve corresponds to a fit of the form $\sum_{i=1}^{3} A_i \exp[-B_i|P_L^{*\gamma}|]$. (See text for further details.) (b) $d\sigma/d|P_L^{*\pi}|$ for the reaction $p+p \to \pi+X$. The curve is the π^0 spectrum derived from the inclusive γ sample. A one-standard deviation uncertainty calculated from the full error matrix of the fit to the γ distribution is shown by the dashed lines bordering the transformed π^0 spectrum. Also shown are inclusive $p+p \to \pi^{\pm}+X$ spectra from Ref. 26. Data points from the inclusive $\pi^0 \to \gamma\gamma$ fits from this experiment are also indicated.

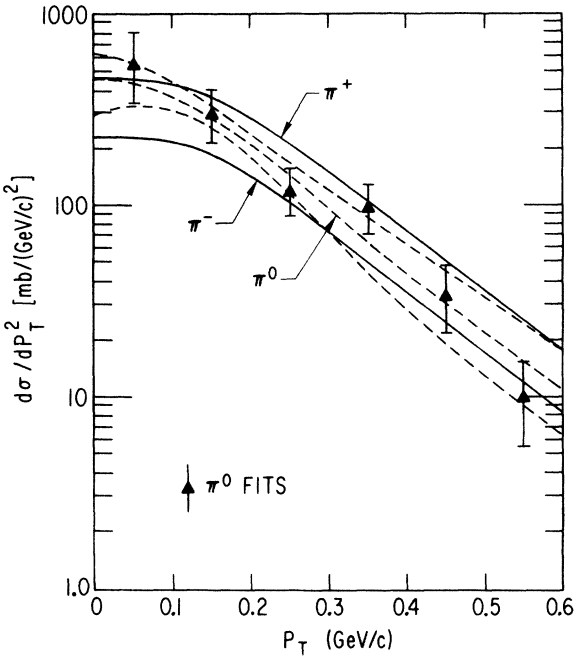

FIG. 19. $d\sigma/dP_T^2$ for the reaction $p+p \to \pi + X$. The broken curves represent the π^0 spectrum, with one-standard deviation uncertainty, derived from the inclusive γ sample. Also shown are inclusive $p+p \to \pi^{\pm} + X$ spectra from Ref. 26. Data points from the inclusive $\pi^0 \to \gamma\gamma$ fits from this experiment are also indicated.

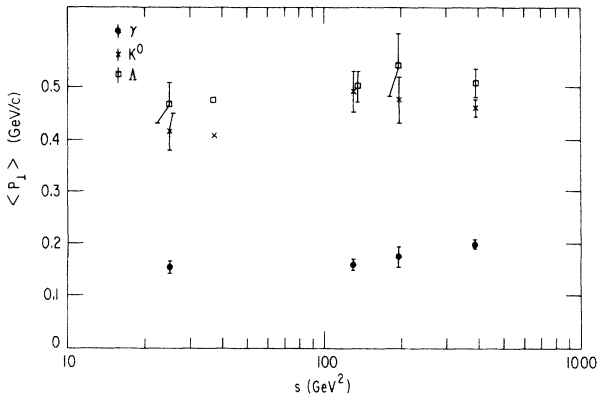

FIG. 20. Average values $\langle P_T \rangle$ for inclusive γ, K^0, and Λ events as a function of s.

ment[26] for the reactions $p+p \to \pi^{\pm} + X$. In both graphs, it is evident that our π^0 cross sections are consistent with being equal to the average of the π^+ and π^- spectra. Lipkin and Peshkin[27] have shown that the relation $d\sigma/dP(\pi^0) = \frac{1}{2}[d\sigma/dP(\pi^+) + d\sigma/dP(\pi^-)]$ should hold at all pion momenta in pp interactions, assuming pure isospin zero t-channel exchange.

In Fig. 20 we show our results for $\langle P_T \rangle$ for inclusive γ, K^0, and Λ production, as well as values found at other energies. In all three cases, there appears to be no significant variation over the energy range indicated. It should be noted, however, that in the case of $pp \to \pi^- + X$, an inclusive channel for which large statistics are available, there is a significant increase with s in $\langle P_T \rangle_{\pi^-}$.[28]

VIII. ASSOCIATED CHARGED MULTIPLICITIES

A study of the charged multiplicity associated with the production of a K^0 or Λ as a function of the $|x|$ and P_T^2 values of the K^0 or Λ are shown in Fig. 21. Figure 21(a) indicates that the average multiplicity seems to be independent of the transverse momentum for both K^0 and Λ production. Figure 21(b) suggests that as a K^0 or Λ is produced nearer to $|x| = 1$, the associated charged particle multiplicity becomes smaller. A similar effect has been observed in 19-GeV/c pp inter-

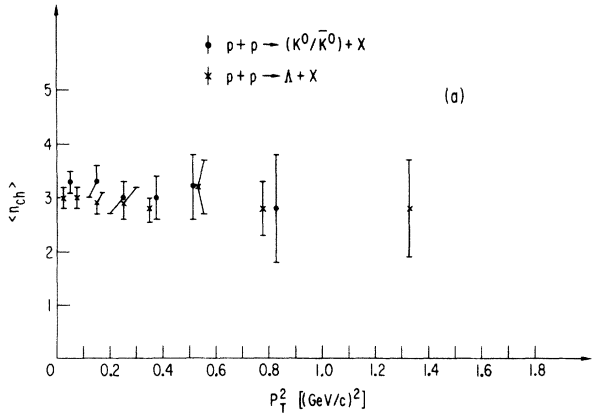

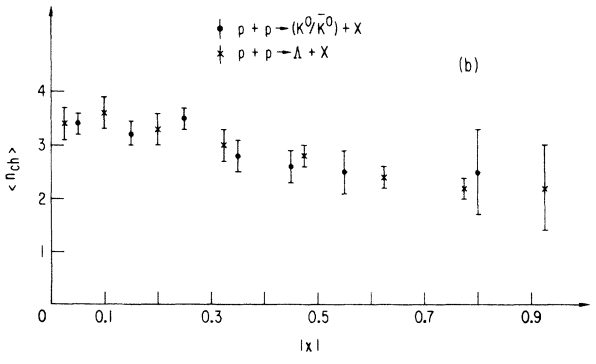

FIG. 21. (a) Average multiplicity for inclusive (Λ) and ($K^0/\bar{K}^0$) events as a function of P_T^2. (b) Same as (a) as a function of $|x|$.

actions.[12]

Figure 22(a) shows the missing mass squared recoiling off a K^0 or Λ in the reactions

$$p + p \to \Lambda + X$$

and

$$p + p \to K^0 + X .$$

Figure 22(b) shows the average associated charged particle multiplicity as a function of $(MM)^2$. Except for the different thresholds associated with these two reactions, we observe no significant differences in the shape of either the $(MM)^2$ or the average multiplicity distribution.

IX. MOMENTUM TRANSFER DISTRIBUTIONS AND POLARIZATION OF THE Λ

A. Momentum transfer distributions

The distribution of momentum transfer, $|t-t_{\min}| = t'$, between the Λ and proton is plotted in Fig. 23. For the events in the forward c.m. hemisphere,

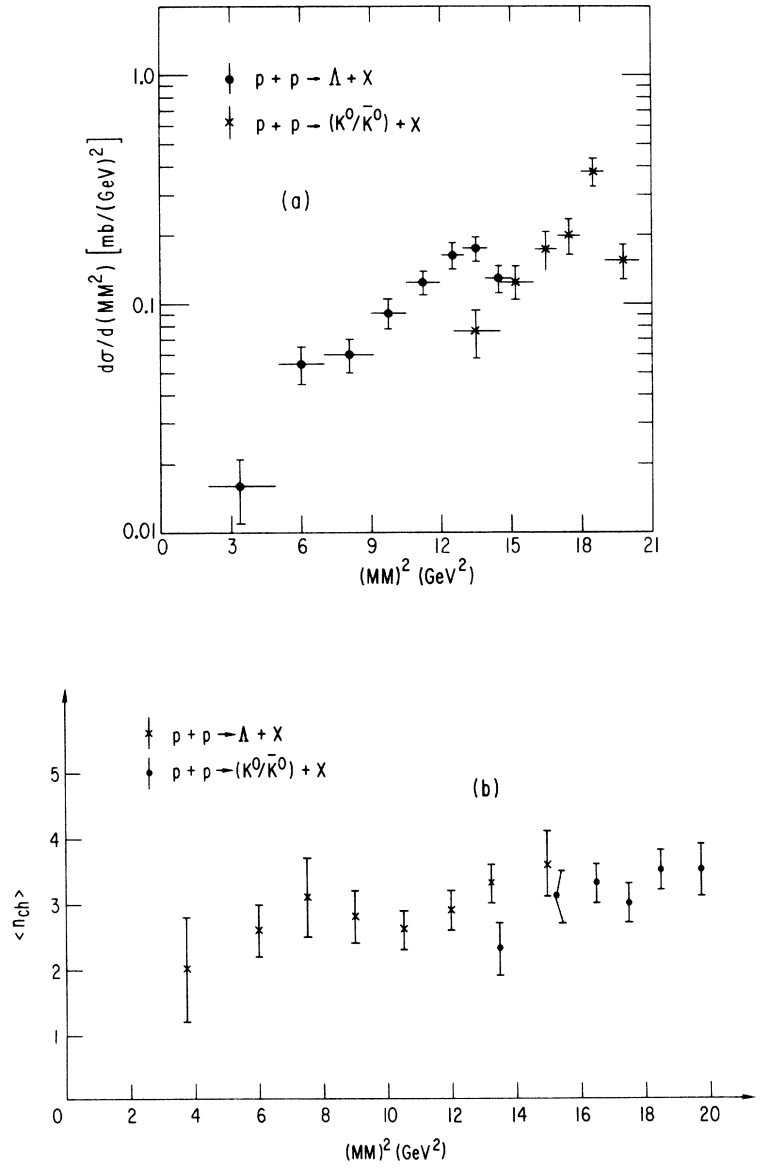

FIG. 22. (a) $d\sigma/d(\mathrm{MM}^2)$ for inclusive (Λ) and ($K^0/\bar{K}^0$) events. (b) Associated charged multiplicity as a function of MM^2 for inclusive (Λ) and ($K^0/\bar{K}^0$) events.

it was calculated between the Λ and the incident proton. For the backward hemisphere, this calculation was made between the Λ and the target proton. The data points were fitted with an exponential

$$\frac{d\sigma}{d|t'|} = A e^{B|t'|},$$

with the following result:

for $0.0 < t' < 1.4$, $A = 1.56 \pm 0.36$ mb/(GeV/c)^2, $B = -(1.57 \pm 0.13)$(GeV/c)$^{-2}$;

for $1.4 < t' < 3.75$, $A = 0.48 \pm 0.20$ mb/(GeV/c)^2, $B = -(0.70 \pm 0.14)$(GeV/c)$^{-2}$.

In the case of the K^0 events, the data are presented in Fig. 24 together with an exponential fit with parameters:

for $0.0 < |t'| < 2.5$, $A = 1.20 \pm 0.48$ mb/(GeV/c)^2, $B = -(0.77 \pm 0.11)$(GeV/c)$^{-2}$.

B. Polarization of the Λ

The polarization of the Λ's is distributed as $W(\cos\theta) = \frac{1}{2}(1 + \alpha P \cos\theta)$, where P = polarization and $\alpha = 0.647$.[9] The angle θ is defined by $\cos\theta = \hat{n} \cdot \hat{p}$, where

$\hat{n}$ = normal to the production plane

$$= \vec{P}_B \times \vec{\Lambda} / |\vec{P}_B \times \vec{\Lambda}|,$$

where $\vec{P}_B$ and $\vec{\Lambda}$ are the momenta of the beam proton and the Λ measured in the laboratory frame, and where $\hat{p}$ is the momentum of the proton from the Λ decay in the Λ rest frame. From the above relation, we then obtain

$$P = \frac{3}{\alpha}\langle\cos\theta\rangle .$$

We obtain (for the average over all events) a polarization of

$$P = -(0.19 \pm 0.15).$$

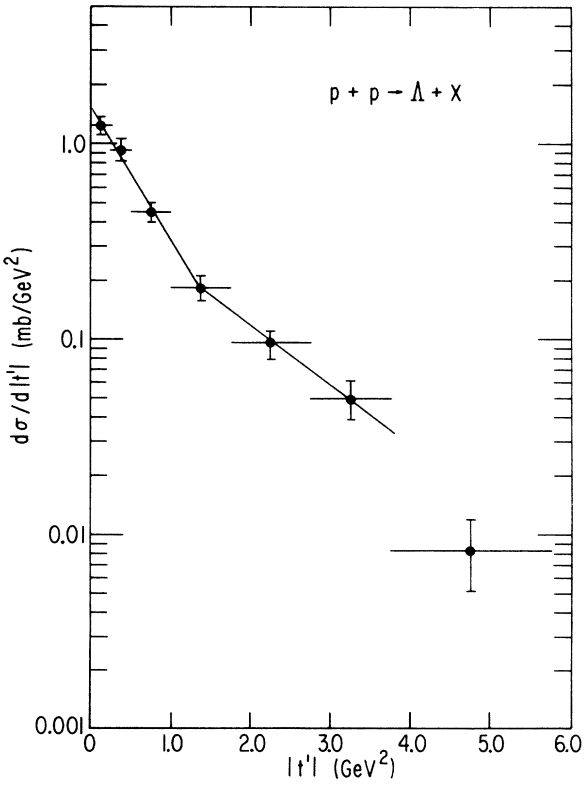

FIG. 23. $d\sigma/d|t'|$ for inclusive Λ events. The curves represent fits to $A \exp(B|t'|)$.

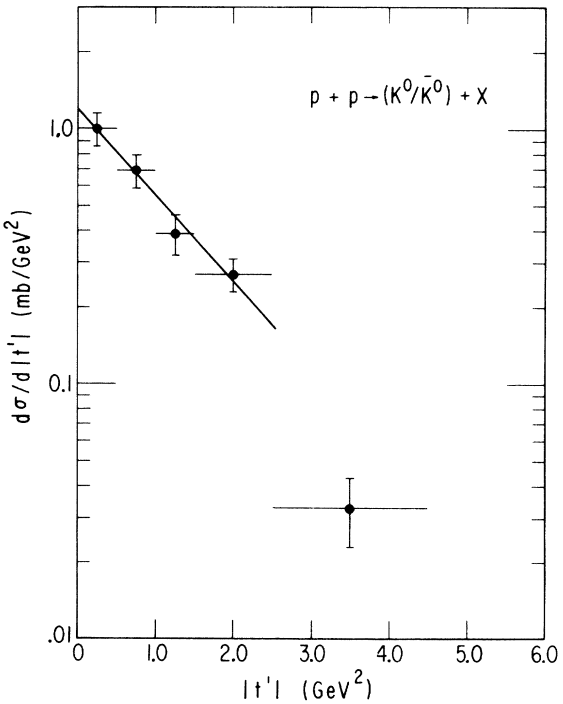

FIG. 24. $d\sigma/d|t'|$ for inclusive $(K^0/\bar{K}^0)$ events. The curve represents a fit to $A \exp(B|t'|)$.

By plotting P as a function of $|x|$, we obtain the graph presented in Fig. 25. It is clear that it is consistent with zero polarization throughout the $|x|$ region. It should be noted, however, that the data include Λ's from Σ^0 decays, a contamination of at most 15%. Hence, zero Λ polarization in this experiment appears to hold true.

ACKNOWLEDGMENTS

We thank the 12-foot bubble chamber personnel for their endurance and support in obtaining the pictures. Many thanks go to our scanning and measuring personnel for their careful work. Our gratitude is extended to the other physicists who worked on this experiment: R. Engelmann, A. Mann, Y. Oren, and P. Peeters. The support and encouragement of M. Derrick, T. H. Fields, and B. Musgrave are greatly appreciated. We are also indebted to E. L. Berger and G. H. Thomas for their helpful advice througout the course of this experiment.

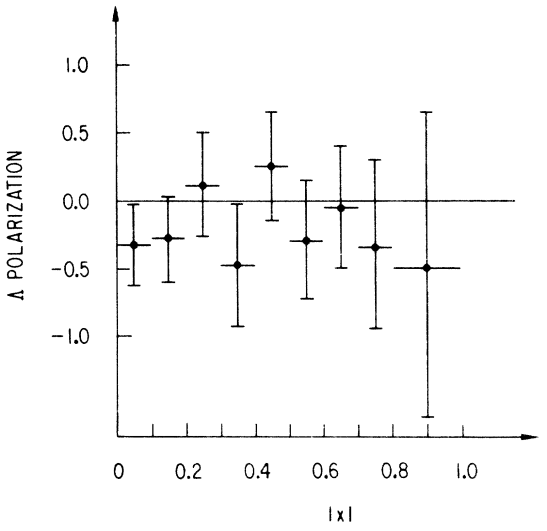

FIG. 25. Polarization of the inclusive Λ events as a function of $|x|$.

*Present address: Singer Company, Kearfott Division, Little Falls, New Jersey 07424.

†Present address: University of Toronto, Toronto, Canada.

‡Work supported by the U. S. Atomic Energy Commission.

§Work supported by the National Science Foundation.

‖Operated by Universities Research Association, Inc. under contract with the U. S. Atomic Energy Commission.

[1]J. H. Campbell *et al.*, Phys. Rev. D 8, 3824 (1973).

[2]D. Swanson *et al.*, Phys. Lett. 48B, 479 (1974).

[3]For further details of this experiment, see D. Swanson, Ph.D. thesis, Illinois Institute of Technology, IIT Technical Report No. 122, ANL/HEP 7352, 1973 (unpublished).

[4]For further details on the 12-foot bubble chamber, see K. Jaeger, ANL/HEP 7210, 1972 (unpublished).

[5]F. Beck, ANL Report No. ANL-HEP 7128, 1971 (unpublished); F. Beck *et al.*, in Proceedings of the Informal Colloquium on POLLY and POLLY-like Devices, ANL Report No. ANL-7934, 1972 (unpublished).

[6]T. M. Knasel, DESY Reports Nos. 70/2 and 70/3, 1970 (unpublished).

[7]Particle Data Group, LBL Report No. UCRL-20000 YN, 1970 (unpublished), p. 17; G. R. Charlton *et al.*, Phys. Lett. 32B, 720 (1970). Above 0.4 GeV/c and up to 5.0 GeV/c, the $\Lambda+p$ cross section is about 35 mb. No values are available above 5.0 GeV/c. We assumed a constant cross section of 35 mb for our calculation, even though the Λ momenta in our experiment range from 0.4 to 11.5 GeV/c.

[8]Even by cutting the primary fiducial volume to $-136 < x < 0.0$ from $-136 < x < 132$, the forward Λ losses still amount to 13%.

[9]Particle Data Group, Phys. Lett. 50B, 1 (1974).

[10]A conservative upper limit on the inclusive Σ^0 cross section was quoted earlier in Ref. 1 as ≤ 1.3 mb. The careful study made for this paper now allows us to quote a more accurate value.

[11]V. Blobel *et al.*, Nucl. Phys. B69, 454 (1974). At 12 GeV/c, $\sigma(p+p \to \pi^0 + X) = 35.2 \pm 2.4$ mb and $\langle \pi^0 \rangle = 1.18 \pm 0.08$; at 24 GeV/$c$, $\sigma(p+p \to \pi^0 + X) = 53.5 \pm 3.1$ mb and $\langle \pi^0 \rangle = 1.75 \pm 0.10$.

[12]H. Bøggild *et al.*, Nucl. Phys. B57, 77 (1973); B27, 285 (1971); private communications with H. Bøggild. At 19 GeV/c, $\sigma(p+p \to \pi^0 + X) = 41.7 \pm 3.0$ mb and $\langle \pi^0 \rangle = 1.4 \pm 0.1$. H. Bøggild *et al.*, Nucl. Phys. B72, 221 (1974).

[13]H. Blumenfeld *et al.*, Phys. Lett. 45B, 525 (1973); 45B, 528 (1973). At 69 GeV/c, $\sigma(p+p \to \pi^0 + X) = 81.1 \pm 4.0$ mb and $\langle \pi^0 \rangle = 2.57 \pm 0.13$.

[14]J. W. Chapman *et al.*, Phys. Lett. 47B, 465 (1973). At 102 GeV/c, $\sigma(p+p \to \pi^0 + X) = 85.0 \pm 8.0$ mb and $\langle \pi^0 \rangle = 2.62 \pm 0.25$.

[15]K. Jaeger *et al.*, Phys. Rev. D. (to be published).

[16]F. T. Dao *et al.*, Phys. Rev. Lett. 30, 1151 (1973); updated at the American Physical Society Washington Meeting, 1974 [Bull. Am. Phys. Soc. 19, 466 (1974)]. At 303 GeV/c, $\sigma(p+p \to \pi^0 + X) = 138.0 \pm 10.0$ mb and $\langle \pi^0 \rangle = 4.21 \pm 0.32$.

[17]A. A. Seidl *et al.*, American Physical Society Washington Meeting, 1974 [Bull. Am. Phys. Soc. 19, 467 (1974)]. At 405 GeV/c, $\sigma(p+p \to \pi^0 + X) = 159.3 \pm 16.8$ mb and $\langle \pi^0 \rangle = 4.86 \pm 0.53$. See also Ref. 14.

[18]G. Neuhofer *et al.*, Phys. Lett. 38B, 51 (1972).

[19]This line is in fact not too different from the curve found at the Intersecting Storage Rings, Ref. 18. They obtained at $\sqrt{s} = 44.7$ GeV a value of $\langle \gamma \rangle = -2.015 \pm 3.013 \ln(\sqrt{s})$. Assuming that $\langle \pi^0 \rangle = \frac{1}{2}\langle \gamma \rangle$, this reduces

to $\langle\pi^0\rangle = -1.008 + 0.754 \ln(s)$, which agrees quite well with the fit shown in Fig. 10.

[20]Data points at various energies were extracted from Ref. 11 (and private communication with H. Fesefeldt), and Refs. 12–16.

[21]At 12.4 GeV/c, the P^*_{max} values are 1.98 GeV/c for $pp \to K^0 + (\Lambda p\pi)$, 2.15 GeV/$c$ for $pp \to \Lambda + (pK)$, 2.16 GeV/c for $pp \to \pi^0 + (pp)$.

[22]R. G. Glasser, Phys. Rev. D 6, 1993 (1972); G. I. Kopylov, Phys. Lett. 41B, 371 (1972); Nucl. Phys. B52, 126 (1973).

[23]For more details on the fitting procedure see Ref. 2. The parameters of the fit to the $|P^{*\gamma}_L|$ data are $A_1 = 309.1 \pm 252.0$ mb/(GeV/c), $A_2 = 364.8 \pm 94.1$ mb/(GeV/c), $A_3 = 91.54 \pm 65.47$ mb/(GeV/c); $B_1 = 46.22 \pm 60.16$ (GeV/c)$^{-1}$, $B_2 = 9.81 \pm 2.78$ (GeV/c)$^{-1}$, $B_3 = 4.28 \pm 0.76$ (GeV/c)$^{-1}$.

[24]The coefficients of this fit are $A_1 = 430.6 \pm 109.1$ mb/(GeV/c), $A_2 = 267.5 \pm 115.6$ mb/(GeV/c); $B_1 = 15.34 \pm 2.72$ (GeV/c)$^{-1}$, $B_2 = 7.68 \pm 0.80$ (GeV/c)$^{-1}$.

[25]R. G. Glasser, Phys. Rev. D 8, 3223 (1973).

[26]The P^*_L and P_y distributions of the $\pi^\pm$ are from the Bonn-Hamburg-München collaboration; private communication from P. Söding. The values for P_T of $\pi^\pm$ are from Ref. 11.

[27]H. J. Lipkin and M. Peshkin, Phys. Rev. Lett. 28, 862 (1972).

[28]J. Whitmore, Phys. Rep. 10C, 328 (1974).